This article has been accepted for publication in a future issue of this journal, but has not been fully edited. Content may change prior to final publication. Citation information: DOI 10.1109/TMI.2020.2989236, IEEE Transactions on Medical Imaging

A Synthetic Total Impulse Response Characterization Method for Correction of Hand-held Optoacoustic Images

Kaushik Basak Chowdhury, Jaya Prakash, Angelos Karlas, Dominik Jüstel and Vasilis Ntziachristos*

***Abstract*— The impulse response of optoacoustic (photoacoustic) tomographic imaging system depends on several system components, the characteristics of which can influence the quality of reconstructed images. The effect of these system components on reconstruction quality have not been considered in detail so far. Here we combine sparse measurements of the total impulse response (TIR) with a geometric acoustic model to obtain a full characterization of the TIR of a handheld optoacoustic tomography system with concave limited-view acquisition geometry. We then use this synthetic TIR to reconstruct data from phantoms and healthy human volunteers, demonstrating improvements in image resolution and fidelity. The higher accuracy of optoacoustic tomographic reconstruction with TIR correction further improves the diagnostic capability of handheld optoacoustic tomographic systems.**

***Index Terms*— Image reconstruction, Photoacoustic tomography, Transducer modelling, Handheld transducer probe, Total impulse response**

I. Introduction

THE quality of tomographic optoacoustic images depends on the accuracy by which the imaging physics, sensor geometry and instrument responses are mathematically modelled in the inversion algorithm employed [1]–[9]. Different components of an optoacoustic tomography system [10], [11] can influence image quality, including the illumination parameters, the ultrasound detector employed or the coupling method used as an interface between tissue and the detector. These influences can be captured by the total impulse response (TIR) of an imaging system, i.e. the convolution of the so-called spatial impulse response (SIR) with the electrical impulse response (EIR). SIR primarily relates to geometrical considerations of sound collection by the detector, whereas the EIR is the impulse response of the transducer design and read electronics of the system. TIR characterization is in general a laborious procedure, where a point absorber has to be scanned on a dense grid throughout the field of view (FOV). EIR can be measured directly if a point absorber is placed exactly at the focus of the transducer element. However, in practice, foci of all the elements of a transducer array are not always at a common point, and it is difficult to perform individual measurements for each transducer focus. Moreover, coupling mismatches between the detector and the tissue imaged may further contribute to image distortions due to wave refraction. Hence, determination of the EIR and TIR of an array transducer represents a critical challenge.

Numerical models may be used to approximate EIR and TIR and offer insights into detector operation. Nevertheless, numerical simulations may contain assumptions and simplifications which do not reflect the actual system modelled and result in loss of image quality. Different aspects of the optoacoustic image reconstruction problem have been investigated to improve image quality; e.g., regularization schemes [12], [13], image/signal processing methods [14], [15] and modelling the underlying physics [16]–[18]. Ideally a suitable combination of all these methods is expected to achieve the best image quality. Since each of these algorithms tend to be computationally expensive, simplifying assumptions like point-like detectors or neglecting the frequency response are often made to lessen the computational burden. However, in many optoacoustic system implementations, both transducer size and bandwidth are significant and can only be neglected at the cost of image quality. Consequently, there is a need for proper characterization of transducer properties [19]–[21]. Finally, acoustic mismatches along the path of ultrasound propagation may also affect image performance, for example acoustic property mismatches between tissue and the coupling medium used to couple the ultrasound detector onto this tissue.

Previous work has examined correction for the EIR in animal systems with large angle of projections [2], [22], [23] showing resolution improvements in the reconstructed images. The effects of SIR correction have also been examined in large projection angle animal imaging systems [2], [9], [24] showing that transducer related artefacts and nearfield artefacts

This project has received funding from the European Research Council (ERC) under the European Union's Horizon 2020 research and innovation programme under grant agreement No 694968 (PREMSOT). J. Prakash acknowledges Alexander von Humboldt Postdoctoral Fellowship program.

K. B. Chowdhury, J. Prakash, A. Karkas, D. Jüstel, and V. Ntziachristos are with Institute of Biological and Medical Imaging, Helmholtz Zentrum Munich, Neuherberg, Germany and Chair of Biological Imaging and TranslaTUM, Technical University of Munich, Munich, Germany.

J. Prakash is also with Dept. of Instrumentation and Applied Physics, Indian Institute of Science, Bengaluru, India.

A. Karkas is also with Clinic for Vascular and Endovascular Surgery, Klinikum rechts der Isar, Munich, Germany.

*Correspondence to V. Ntziachristos (E-Mail: v.ntziachristos@tum.de)

were reduced improving the quality of image reconstruction. Also, an optimal post-filtering technique [25] was proposed to decrease the effect of the finite size of the transducer. In addition to examining the individual contributions of EIR and SIR, a TIR correction scheme was also considered for full view animal systems under the assumption of constant acoustic speed [2] and demonstrated improvement of spatial resolution and mitigation of transducer aperture size related artefacts in the reconstructed images. While work with full-projection animal systems has demonstrated image quality improvements after EIR, SIR or TIR correction, there are currently no systematic studies that model refraction effects and perform TIR correction in limited view acquisition geometries [26]–[29] used for clinical handheld imaging. As handheld optoacoustics is increasingly considered for clinical studies [29]–[35], the investigation and possible correction for TIR effects becomes particularly important, in particular as it relates to delivering high-fidelity quantitative images.

In this work, we aim at a decomposition of the TIR into its different components, so that we can separately study the refraction effects of the coupling medium, the spatial sensitivity field of the transducer array and the acousto-electric response of the transducer on the impulse response of the system. In particular, we hypothesized that refraction effects play a major role in image quality and their correction could lead to a more accurate model of SIR.

To achieve this goal, we introduce a method to characterize the TIR of a clinical handheld optoacoustic system by combining a few measurements of the TIR with a detailed mathematical model. The proposed method bypasses the difficulties of measuring TIR on dense grids within the FOV. We call this TIR model synthetic TIR (sTIR), as it is synthesized from experiments and theoretical considerations. In particular, the method provides an explicit decomposition of sTIR into simulated SIR and approximate EIR. The sTIR model is applicable in situations with a significant mismatch in the acoustic properties of coupling medium and sample, which is, for example, the case when using heavy water as coupling medium for imaging biological tissue. We give a detailed analysis of how refraction at the interface between coupling medium and sample influences the SIR of the system.

We included the sTIR model into a model-based reconstruction algorithm to study the improvement in optoacoustic images throughout the FOV. More precisely, to study the influence of the different components of sTIR, we employed six different forward models with different combinations of these components. Experimental measurements and modelling parameters were based on a clinical handheld optoacoustic device with limited projection angle geometry. The improvement in optoacoustic image quality is demonstrated with measurements from phantoms and in-vivo, from the human forearm. We discuss the individual effects of correcting for refraction effects, simulated SIR and approximate EIR in detail.

In see Section II, we briefly review acoustic refraction, propagation models including the integration of TIR and model-based reconstruction methodology. In see Section III, we give the details of our sTIR model that synthesizes TIR from sparse measurements and an SIR model. In Section IV, we demonstrate improvement in image quality using sTIR models. Finally, section V discusses the major findings and advantages of the proposed sTIR characterization and reconstruction method.

II. Theory and Methods

The central goal of this work is to characterize the TIR of a handheld optoacoustic system in the entire field of view. However, an explicit measurement of the TIR in all points within the FOV is time consuming, prone to various experimental errors and may be confounded by technical constraints associated with long measurement times, such as laser overheating. In order to address this challenge, we derive a detailed TIR model and propose a technique to synthesize the system TIR by combining this model with measurements of the TIR in a few selected locations. In particular, this method allows to characterize the approximate EIR of the transducer elements.

A. Theory

The optoacoustic wave equation [36] assuming a lossless homogeneous medium can be written as

$$\frac{\partial^2 p(r,t)}{\partial t^2} - c_0 \nabla^2 p(r,t) = \Gamma \frac{\partial H(r,t)}{\partial t}, \tag{1}$$

where $p(r,t)$ is the observed pressure at location r, and at time t. H is the heating function which indicates the amount of energy deposited in the sample per unit volume per unit time, c_0 is the acoustic speed in the medium, which we assume to be constant and Γ is the dimensionless Grüneisen parameter [37], which we also assume to be constant. Using the free space Green's function, the solution of this inhomogeneous optoacoustic wave equation can be written as [37],

$$p(r,t) = \frac{\Gamma}{4\pi} \int \frac{dr'}{|r-r'|} \frac{\partial}{\partial t'} H(r',t') \bigg|_{t'=t-|r-r'|/c_0}. \tag{2}$$

In time domain optoacoustic imaging, the requirement for thermal confinement [37] is satisfied when the laser illumination pulse duration is short enough that heat conduction into neighboring regions of the illuminated region can be neglected. Hence, temporal heating is instantaneous and can be approximated by a Dirac delta δ such that $H(r,t) = H_r(r)\delta(t)$, and Eq. (2) takes the form

$$p(r,t) = \frac{\Gamma}{4\pi} \frac{\partial}{\partial t} \int \frac{H_r(r')}{|r-r'|} \delta\left(t - \frac{|r-r'|}{c_0}\right) dr', \tag{3}$$

which can be used to determine the optoacoustic pressure generated by the energy H_r absorbed by any optically absorbing object. The integral in (3) describes the accumulation of the optoacoustic pressure waves $p(r,t)$ recorded by an ideal point detector located at r due to the excitation of point-like absorbers located at r'. The challenge for quantitative optoacoustic image reconstruction is to determine the optical absorption distribution μ_a from the measured pressure $p(r,t)$ at all detector locations r. This can be done in two steps: acoustic inversion, where the initial pressure p_0 is estimated

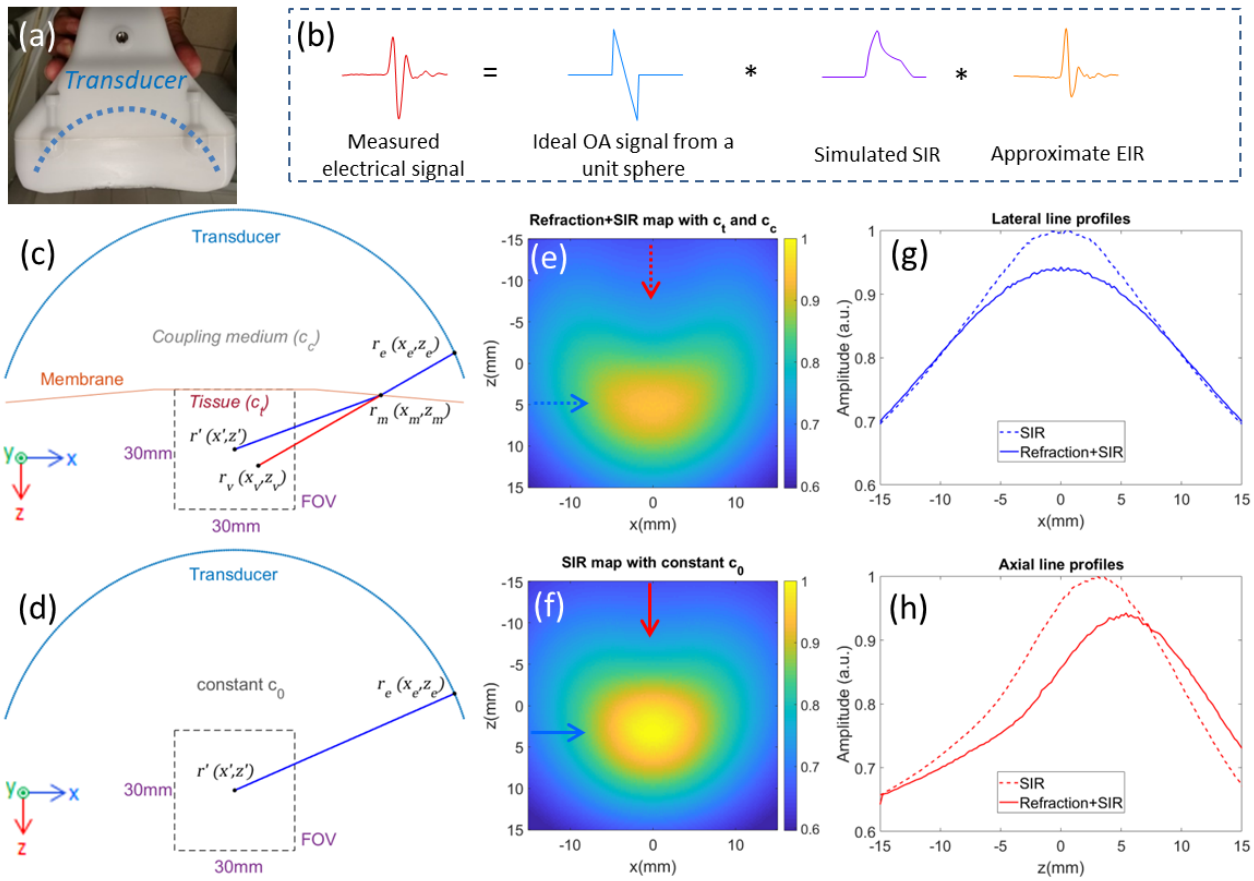

Fig. 1. Model of the optoacoustic handheld probe. (a) Photograph of the optoacoustic handheld probe. (b) Decomposition of the detected pressure signal showing the signal components - Ideal OA signal, simulated SIR and approximate EIR which are temporally convolved. (c) Schematic of the refraction model of the optoacoustic handheld probe. (d) Schematic of constant acoustic speed model of the optoacoustic handheld probe. (e) SIR map with refraction model of transducer array (red arrow and blue arrows indicating axial and lateral profiles respectively). (f) SIR map with constant acoustic speed model of transducer array (red arrow and blue arrows indicating axial and lateral profiles respectively). (g) Axial line profiles comparing SIR in constant acoustic speed model (dashed line) and SIR in refraction model (solid line). (h) Lateral line profiles comparing SIR in constant acoustic speed model (dashed line) and SIR in refraction model (solid line). EIR, electrical impulse response; FOV, field of view; OA, optoacoustic; SIR, spatial impulse response.

from (3) and the relation $p_0 = \Gamma H_r$; followed by optical inversion, where the absorption coefficient μ_a is inferred from the initial pressure via $p_0 = \Gamma \mu_a \phi$, where ϕ is the light fluence distribution. The initial pressure p_0 propagates through the coupling medium, is intercepted by the transducer's active surface and gets converted to an electrical signals s. This forward mapping can be written as $s = M^{TIR}(p_0)$ where M^{TIR} is an operator modelling the TIR, which we assume to be linear. Fig. 1b represents how the pressure signal is transformed into a measured electrical signal through temporal convolution with SIR and EIR. This paper will only be concerned with the characterization of the TIR and its application to the acoustic inversion problem. Since optoacoustic wave detection (3) is linear, the measurement operator can be discretized in the form of matrices [38] and the forward model of optoacoustic imaging can be written as

$$s = Mf, \tag{4}$$

where M is the forward model matrix that maps the initial pressure f in arbitrary units to the recorded signal vector s. This forward model including TIR, has so far been implemented in reconstruction methods that assume constant acoustic speed [2], [24] and so are incapable of producing accurate reconstructions when the acoustic mismatch between the sample and coupling agent is substantial.

B. TIR models for refraction at an interface

We start by modelling refraction effects, then derive the SIR in this context and finally include EIR to obtain the full TIR model. Fig. 1a shows a photograph of the handheld probe with the curved array transducer indicated by a dotted blue line. Fig. 1c shows each transducer element is cylindrically focused onto the image plane, which is the xz-plane. The image is discretized into a collection of $P \times P$ uniform spheres(pixels) with diameter D in a Cartesian grid with spacing D, as described in [2], [39]. The general normalized analytical 'N'-shaped optoacoustic pressure wave [39] generated by a uniform spherical absorber of diameter D in a medium with acoustic speed c, is given by

$$p_c^N(t) = \begin{cases} -t & |t| \le \frac{D}{2c}, \\ 0 & \text{elsewhere.} \end{cases} \tag{5}$$

1) Acoustic refraction: Fig. 1c visualizes acoustic refraction at a membrane acting as an interface between coupling medium and tissue. An acoustic wave originating from the tissue with acoustic speed c_t undergoes refraction at this membrane interface and propagates with acoustic speed c_c in coupling medium, finally reaching the transducer element at r_e. To calculate the time-of-flight of the refracted ray as depicted by the blue solid line in Fig. 1c, we utilize Fermat's principle of least time. For a given pair of (r', r_e), we find the point of incidence r_m on the membrane by minimizing the total time-of-flight along the refracted ray $(r' - r_m - r_e)$:

$$r^m_{c_c,c_t}(r_e, r') = \arg\min_{r_m \in \mu} \frac{|r_e - r_m|}{c_c} + \frac{|r_m - r'|}{c_t}, \tag{6}$$

where $r^m_{c_c,c_t}(r_e, r')$ indicates the dependencies of r_m, and μ denotes the set of all points on the intersection of image plane and membrane surface. Then the optimal time-of-flight for the refracted ray is

$$t_{c_c,c_t}(r_e, r') = \frac{|r_e - r^m_{c_c,c_t}(r_e, r')|}{c_c} + \frac{|r^m_{c_c,c_t}(r_e, r') - r'|}{c_t}. \tag{7}$$

The minimization in (6) was performed using the golden section search and parabolic interpolation [40], [41] which enables us to find the minimizer of the single variable function within a specified bound which is the membrane model. Other optimization schemes, like Fletcher-Reeves or Newton type schemes can also be used. The optoacoustic signal generated in tissue by a pixel (modelled as a solid uniformly absorbing sphere) at r' that is detected by an ideal point-like transducer with infinite detection bandwidth located at r_e in the coupling medium is given by

$$s_{r_e,r'}(t) = f_{r'} \cdot p^N_{c_c}(t - t_{c_c,c_t}(r_e, r')), \tag{8}$$

where $\cdot$ denotes scalar multiplication. The assumption underlying this model is, that the wave shape does not change due to refraction. Since, the transducer used in this study is responsive only in a very short range (2 - 7 MHz) of ultrasound frequency range, the acoustic dispersion [42], [43] phenomenon being weak can be neglected in our case.

2) Refraction based SIR: As shown in Fig. 1c, when an optoacoustic response originates from a point source at a location r' within the sample and is refracted, the signal propagates towards the detector r_e along a different direction than directly from its origin. After the refraction event, it propagates along the direction $(r_e - r_m)/|r_e - r_m|$ from r_m towards r_e. Since the distance between membrane and detector is significantly greater than the width of the transducer element, the variation of the point r_m with respect to the interception point on the transducer surface can be neglected. Consequently, the wave is intercepted at the transducer element as if it originated from a virtual source located at a point r_v in the direction of r_m at a distance corresponding to the time of flight and travelled at the coupling speed of sound c_c along a straight line without being refracted. More precisely, the location of the virtual point source is given by

$$r^v_{c_c,c_t}(r_e, r') = r_e - c_c \cdot t_{c_c,c_t}(r_e, r') \cdot \frac{r_e - r_m}{|r_e - r_m|}. \tag{9}$$

For readability we abbreviate $r_v = r^v_{c_c,c_t}(r_e, r')$ to denote the virtual point. Note, that $r_v = r'$ when $c_c = c_t$. The SIR $h^{SIR}_{c_c,c_t,r_e,r'}$ for an impulse originating at r' and travelling to the element r_e along the refracted path at the two different acoustic speeds c_c and c_t is thus identical to the SIR $h^{SIR}_{c_c,r_e,r'}$ for an impulse originating at the virtual point r_v and travelling along a straight line with the constant acoustic speed c_c of the coupling medium. In summary, the optoacoustic signal generated in tissue by a uniform absorbing sphere at r', detected by a transducer element with finite active surface area S_e and infinite detection bandwidth located at r_e, can be written as

$$s_{r_e,r'}(t) = f_{r'} \cdot h^{SIR}_{c_c,c_t,r_e,r'} * p^N_{c_c}(t - t_{c_c,c_t}(r_e, r')), \tag{10}$$

where $*$ denotes temporal convolution. The refraction-based SIR is given by

$$h^{SIR}_{c_c,c_t,r_e,r'}(t - t_{c_c,c_t}(r_e, r')) = \int_{S_e} \frac{\delta\left(t - \frac{|s - r_v|}{c_c}\right)}{|s - r_v|} dS(s). \tag{11}$$

Adding $h^{EIR}_{r_e}$ to (10), we get the composite signal detected by a transducer:

$$s_{r_e,r'}(t) = f_{r'} \cdot h^{EIR}_{r_e} * h^{SIR}_{c_c,c_t,r_e,r'} * p^N_{c_c}(t - t_{c_c,c_t}(r_e, r')), \tag{12}$$

Note, that (12) simplifies to case for constant acoustic speed $c_0 = c_c = c_t$ (model shown in Fig. 1d). The continuous pressure signal $s_{r_e,r'}$ in (12) is sampled at the discrete times $t = n \cdot \Delta t$, where $n = 0, 1, ..., (T-1)$ and Δt is the sampling interval. Denoting the time index corresponding to the travel time along the refracted path by n_R , we can write

$$s_{r_e}[n] = \sum_{r' \in FOV} f_{r'} \cdot m_{r_e,r'}[n - n_R], \tag{13}$$

where,

$$m_{r_e,r'}[n] = h^{EIR}_{r_e} * h^{SIR}_{c_c,c_t,r_e,r'} * p^N_{c_c}[n], \tag{14}$$

is the normalized contribution of a single spherical absorber at location $r' \in FOV$.

The pressure signal is recorded at the N locations of the transducer elements indexed by $r_e = 1, 2, ..., N$. The location of the uniform spherical absorber r' in the FOV can be indexed by (i, j) where $i = 1, 2, ..., P$; $j = 1, 2, ..., P$, such that P^2 is the total number of uniform spherical absorbers in the FOV. Hence, (13) can be expressed in a matrix relation as

$$\begin{bmatrix} s_1 \\ s_2 \\ \vdots \\ s_N \end{bmatrix} = \begin{bmatrix} m_{1(1,1)} & m_{1(2,1)} & \cdots & m_{1(P,P)} \\ m_{2(1,1)} & m_{2(2,1)} & \cdots & m_{2(P,P)} \\ \vdots & \vdots & \ddots & \vdots \\ m_{N(1,1)} & m_{N(2,1)} & \cdots & m_{N(P,P)} \end{bmatrix} \begin{bmatrix} f_{(1,1)} \\ f_{(2,1)} \\ \vdots \\ f_{(P,P)} \end{bmatrix} \tag{15}$$

or,

$$s = Mf, \tag{16}$$

where, $M = [m_{r_e(i,j)}]$ is the model matrix. Equations (5)-(7), (9), (11)-(15) comprise the complete model for the acoustic data acquisition for refraction at an interface.

This article has been accepted for publication in a future issue of this journal, but has not been fully edited. Content may change prior to final publication. Citation information: DOI 10.1109/TMI.2020.2989236, IEEE Transactions on Medical Imaging

III. Simulation and Experiments

A. Synthetic TIR(sTIR)

In the previous subsection we formulated the general forward TIR model. We now use this model to derive a characterization of the TIR of a clinical handheld optoacoustic system in the whole image plane. This TIR will be called synthetic TIR (sTIR), because we synthesize it from a few experimental measurements of the system TIR and our theoretical TIR model. The synthesis is performed in four steps: 1) measurements of TIR in a few locations in the FOV, 2) numerical simulation of the SIR model, 3) extraction of approximate EIR by combining the measurements and the simulations with the model, 4) generation of sTIR in the whole FOV by combining the simulated SIR with the derived approximate EIR. In the following we discuss each step involved in generating the sTIR in detail.

1) TIR measurements: We recorded the optoacoustic signals generated by a single polyethylene microsphere of diameter 100 µm, placing it at 11 × 11 grid locations spaced 3 mm apart in the FOV, immersing the handheld scanner in a water bath as shown in Fig. 3b,c. Note, that the measured optoacoustic signals contain the TIR of each location of the microsphere.

2) Refraction based SIR simulation: We introduced the concept of virtual point to tackle the dependence of SIR on refraction. As mentioned before the transducer used is narrowband and hence, we can assume that the travelling acoustic wave shape is not altered after refraction across membrane. Therefore, the proposed SIR model depends only on the relative position of the virtual point and the detector. We can efficiently [44] use Field II package [45] considering the virtual point as the origin of acoustic impulse and acoustic propagation speed set to 1397 m/s [46], which is the speed of sound in the coupling medium (heavy water) at room temperature. The active surface area of each transducer element was discretized into small square sub-apertures of dimension 50 µm × 50 µm, which was sufficient for the exploited scanning geometry [45]. To visualize the SIR in the FOV, we plotted the square root of the energy of the SIR at each pixel and obtained the sensitivity maps in Fig. 1e,f. Fig. 1e shows the SIR map of the transducer array considering refraction at the membrane with acoustic speed in coupling medium as c_c = 1397 m/s and average acoustic speed in tissue [47] as c_t = 1540 m/s as shown in Fig. 1c. Likewise, Fig. 1f shows the SIR map of the transducer array considering constant acoustic speed c_0= 1470 m/s corresponding to the constant acoustic speed model shown in Fig. 1d. We observe that there is a significant distortion in the SIR map due to refraction of acoustic waves at the membrane. Fig. 1g,h shows the axial (red) and lateral (blue) profiles across the highest sensitivity region of the SIR map with constant acoustic speed (dashed line) and the SIR map with refraction (solid line). As a result of the refraction, the SIR map is shifted in the axial direction and spread across the lateral direction, and sensitivity is reduced. This indicates the importance of considering the refraction while computing SIR for a transducer array enclosed within a probe containing a coupling medium with significantly different acoustic properties than the biological tissue to be imaged.

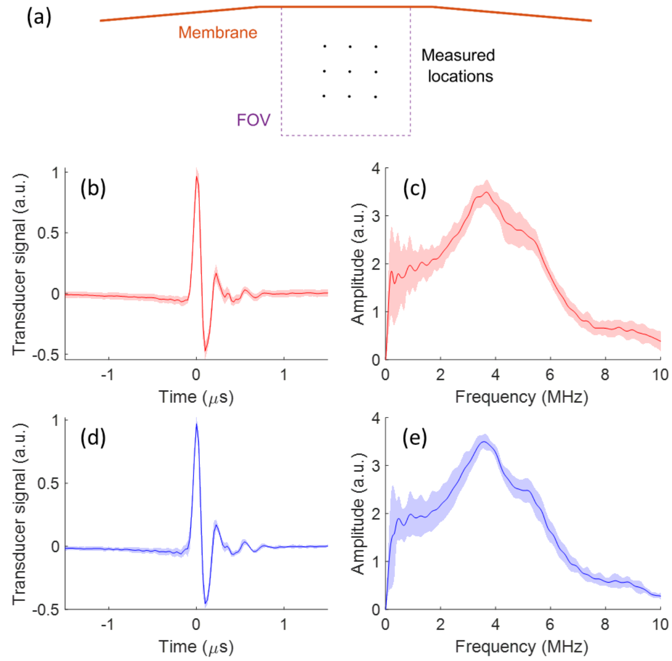

Fig. 2. Experimentally derived approximate EIR (or aEIR) and validation of simulated SIR. (a) Measurement locations inside the FOV to validate accuracy of simulated SIR. (b-c) aEIR over all elements measured at single location at center of FOV in time and frequency domains respectively. (d-e) aEIR across different locations of the FOV in time and frequency domains respectively. Solid lines indicate mean values, while the surrounding shading indicates the standard deviation.

3) Approximate EIR derivation: We extract the approximate EIR of our optoacoustic transducer probe from the measured signals containing the TIR and our simulated refraction based SIR. We refer to the derived EIR as approximate EIR (or aEIR) because the derived EIR will have effects of the imaging system (like fluence, source profile, Grüneisen parameter, etc) that are not accounted for. In order to reduce the contamination of SIR we choose a TIR measurement and SIR simulation at a point located approximately in the the center of the FOV. This was done in accordance with the known fact that the effect of SIR is least close to the focus [2], [24], [48].

In agreement with our TIR measurements of the response of a polyethylene microsphere of diameter 100 µm, we use a normalized 'N'-shaped optoacoustic response from a homogenous solid sphere of diameter D = 100 µm in (13)-(14). The experimentally measured signal at element e can be written as

$$s_{r_e,r'}[n] = f_{r'} \cdot h^{aEIR}_{r_e} * m^{R}_{r_e,r'}[n - n_R], \qquad (17)$$

where,

$$m^{R}_{r_e,r'}[n] = h^{SIR}_{c_c,c_t,r_e,r'} * p^{N}_{c_c}[n - n_R], \qquad (18)$$

is the response of the microsphere including SIR, but before being subject to the system aEIR. Equation (17) suggests deriving aEIR from the measurements of $s_{r_e,r'}$ by deconvolution with respect to the simulations of $m^{R}_{r_e,r'}$. We performed this deconvolution numerically via a Wiener filter and an estimate of the Gaussian noise with 0.1 as nsr (noise to signal power ratio) in MATLAB. As the transducer elements are assumed

TABLE I
THE SIX CONSIDERED FORWARD MODELS FOR CONSTANT ACOUSTIC SPEED AND REFRACTION WITH SIR AND STIR CORRECTIONS. THE ENTRIES OF THE TABLE SHOW THE FORM OF THE CORRESPONDING MATRIX ELEMENTS

$\boldsymbol{M}$	M_x $h^{SIR}=\delta; h^{aEIR}=\delta$	M_x^{SIR} (SIR correction); $h^{aEIR}=\delta$	M_x^{sTIR} (sTIR correction)
M_0^x	$p_{c_0}^N[n-n_0]$	$h_{c_0,r_e,r'}^{SIR} * p_{c_0}^N[n-n_0]$	$h_{r_e}^{aEIR} * h_{c_0,r_e,r'}^{SIR} * p_{c_0}^N[n-n_0]$
M_R^x	$p_{c_c}^N[n-n_R]$	$h_{c_c,c_t,r_e,r'}^{SIR} * p_{c_c}^N[n-n_R]$	$h_{r_e}^{aEIR} * h_{c_c,c_t,r_e,r'}^{SIR} * p_{c_c}^N[n-n_R]$

to be identical, the aEIR of the whole transducer array can be approximated by the average over all the elements and can be expressed as

$$h^{aEIR}[n] = \frac{1}{N_e}\sum_{e=1}^{N_e} h_{r_e}^{aEIR}[n]. \quad (19)$$

Fig. 2b-c, shows the aEIR computed at the center of FOV in the image plane across different transducer elements; the solid red line represents the mean and the red shading represents the standard deviation at each time/frequency point.

More precisely, to verify the accuracy of the simulated SIR we investigated the variation of the derived aEIR from different locations in the FOV as shown in Fig. 2a. Since EIR depends only on the electro-acoustic properties of the transducer element and not on the relative location of the source of the acoustic impulse, we expect the derived aEIR to be independent of the location in the image plane. In order to verify this, we computed h_{aEIR} for 9 different locations in the image plane and found that they are consistent having a Coefficient of Variation (CV) ≤ 0.05, as shown in Fig. 2d-e, where the bold blue line is the mean and the blue shading visualizes the standard deviation at each time/frequency point. The low variance of the aEIR indicates that the simulated SIR can reliably be used over the entire FOV. It also quantifies the aforementioned uncertainties.

4) Synthesis of sTIR: Finally, we combine the derived aEIR (19) with the simulations of SIR (11) to obtain the sTIR in the whole field of view. More precisely, sTIR forward model is given by

$$s_{r_e}[n] = \sum_{r'\in FOV} f_{r'} \cdot h^{aEIR} * h_{c_c,c_t,r_e,r'}^{SIR} * p_{c_c}^N[n-n_R], \quad (20)$$

5) Forward models: We consider six different forward models in order to systematically study the effect of the components of the sTIR sequentially - refraction, SIR and aEIR, from the generation of acoustic waves until their conversion to electrical signals.

Using (5)-(14), we propose three different refraction-based forward models for reconstruction: M_R for an ideal point detector, M_R^{SIR} including SIR, and M_R^{sTIR} including sTIR. These models are shown in the second row of Table 1, named M_R^x. In order to compare our refraction based forward models with those of existing forward models based on constant acoustic speed, we use $c_0 = c_c = c_t$ in (5)-(14) and consider three models for constant acoustic speed: M_0 for an ideal point detector, M_0^{SIR} including SIR, and M_0^{sTIR} including sTIR. These three models are shown in in the first row of Table I, named M_0^x.

Building the forward model is a one-time effort, and (6) must be solved $P^2 \times N$ times. For 151 $\times$ 301 pixels and 256 elements transducer array. The time required to compute the different M_R and M_R^{SIR}/M_R^{sTIR} models are approximately 1hr and 3hrs, respectively, on a computer with Intel(R) Core (TM) i7-6700K CPU @ 4.00 GHz. Once the forward model is built, each reconstruction takes around 40 seconds.

B. Image correction using sTIR

The generated sTIR can be used in the forward models (mentioned in Table I) to correct images using the model-based image reconstruction framework. We also report the design of numerical and physical phantoms used for experiments and details of the experimental setup used for generating the results.

1) Image reconstruction framework: The acquired signals were first preprocessed with a Butterworth bandpass filter in the frequency range of 100 kHz to 12 MHz to reject noise beyond the sensitivity of the transducer. In order to demonstrate SIR and sTIR correction in constant acoustic speed models and refraction models step-by-step, we used the six different forward models in Table I to reconstruct the optoacoustic images. Since ideally EIR is independent of the locations of transducer element and the origin of the impulse, aEIR correction can be performed as a preprocessing step by deconvolution of the measured signals with respect to the derived aEIR h_{aEIR}. This deconvolution was again performed numerically via a Wiener filter and a Gaussian noise model with 0.1 being noise to signal power ratio. The general forward model can be expressed as

$$s' = \boldsymbol{M}f, \quad (21)$$

where s' is the column vector of the pre-processed signals. For the signals with and without aEIR deconvolution we write s^d and s, respectively. The different model matrices are denoted by $\boldsymbol{M} \in \{M_R, M_R^{SIR}, M_0, M_0^{SIR}\}$. Equation (21) is solved for the optoacoustic image f by solving the regularized least squares problem

$$f_{sol} = \arg\min_f \|\boldsymbol{M}f - s'\|_2^2 + \lambda\|Lf\|_2^2, \quad (22)$$

where L is the identity matrix as we used the standard form of Tikhonov regularization. We have used an LSQR-type method to choose the regularization parameter [49], [50], which is based on the simplex method. The addition of SIR and aEIR increases the size of the forward model matrix making it prohibitive to use L-curve or GCV based automatic choice of regularization parameter due to the huge computationally cost associate with these methods. Since

This article has been accepted for publication in a future issue of this journal, but has not been fully edited. Content may change prior to final publication. Citation information: DOI 10.1109/TMI.2020.2989236, IEEE Transactions on Medical Imaging

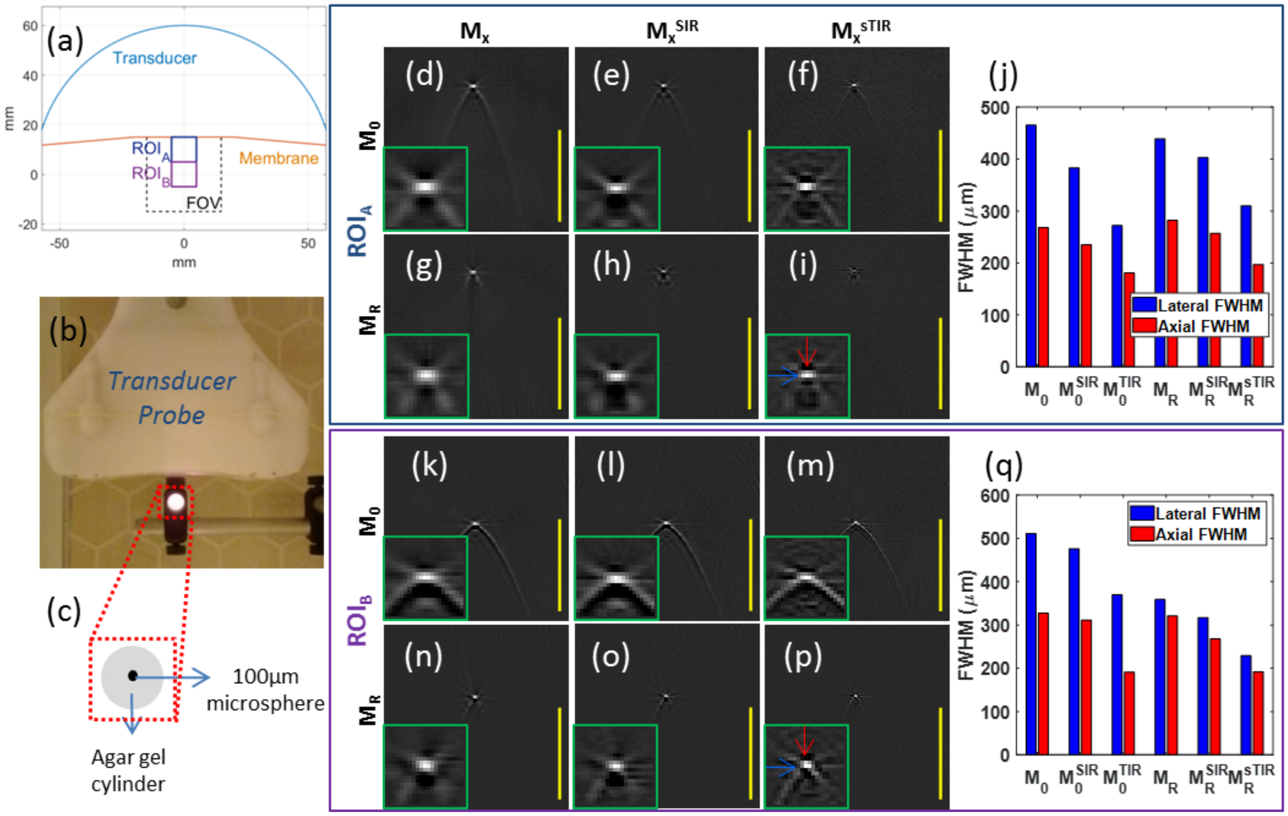

Fig. 3. Improvement in system resolution through correcting for refraction and transducer properties. A microsphere with a diameter of 100 µm was embedded in an agar cylinder and scanned in the FOV of the handheld probe immersed in water using a single excitation wavelength of 700 nm. (a) Schematic of the probe showing ROI_A and ROI_B, each measuring 10 x 10 mm, inside the FOV (30 x 30 mm). (b) Photograph of the microsphere phantom being scanned with the handheld probe. (c) Schematic of the microsphere phantom. (d-i) Images of the microsphere located in ROI_A reconstructed using the M_0 forward model (upper row) or M_R forward model (lower row) in the absence of transducer correction geometry (left column), with SIR correction (middle column) or sTIR correction (right column). The red and blue arrows indicate axial and lateral line profiles. A higher-magnification view of the microsphere is shown as an inset. (j) Comparison of lateral FWHM and axial FWHM in images at ROI_A. (k-p) Images of the microsphere located in ROI_B reconstructed using the M_0 forward model (upper row) or M_R forward model (lower row) in the absence of transducer correction geometry (left column), with SIR correction (middle column) or sTIR correction (right column). The red and blue arrows indicate axial and lateral line profiles. A higher-magnification view of the microsphere is shown as an inset. (q) Comparison of lateral FWHM and axial FWHM in images at ROI_B. Scale bar, 5 mm.

the regularization parameter was chosen semi-automatically, there was no bias introduced while comparing the different reconstructions schemes. Illustration of semi-automatic choice of regularization parameter is provided in Supplementary Fig. 4.

2) Numerical phantom studies: The proposed reconstruction method was tested using a dot grid numerical phantom (shown in Fig. 4a) to demonstrate the negative effects on image quality due to neglecting transducer properties. Additional test results using a numerically simulated USAF chart are provided in Supplementary Fig. 1. To avoid the inverse crime, we used a high resolution (100µm over the 30mm FOV) ground truth of the numerical phantoms and signals were obtained using the sTIR model matrix M_R^{sTIR}. In addition, different levels of noise were added in order to obtain noisy optoacoustic signals with SNR ranging from 40dB to 5dB (provided in Supplementary Fig. 2). All reconstructions of numerical phantoms are performed in a coarse resolution (close to system resolution) of 200µm over the 30mm FOV. The Structural Similarity Index (SSIM) [51], which is based on visual perception of shapes and structures, was used to evaluate the reconstruction performance in experiments where ground truths were available. The SSIM with respect to the ground truth was computed after normalizing images by their maxima and discarding negative values, which represent unreal optoacoustic contrast. The reconstructed images were normalized before computing SSIM because the ground truths were generated in the range [0, 1]. The reported SSIM values lie in the reasonable range [0, 1]. Reconstructions in Fig. 4. are obtained from non-noisy signals and reconstruction results for the USAF chart (Supplementary Fig. 1) are obtained using noisy signals with SNR of 20dB.

3) Experimental measurements: The optoacoustic imaging platform employed for experimental tests and validation of the proposed reconstruction method was previously described [52]. In brief, a tunable (680-980 nm) pulsed laser (Spitlight 600 DPSS, Innolas Laser, Germany) with pulse length around 8 ns operating at 50 Hz was used as the illumination source. The light was delivered using a custom-made fiber bundle (CeramOptec, Germany) along a line 40 mm $\times$ 1 mm at the output in the handheld probe. The transducer used in this handheld probe is slightly different from the ones used in previous handheld multispectral optoacoustic (MSOT) scanners [52], [53]. In the present work, the generated optoacoustic

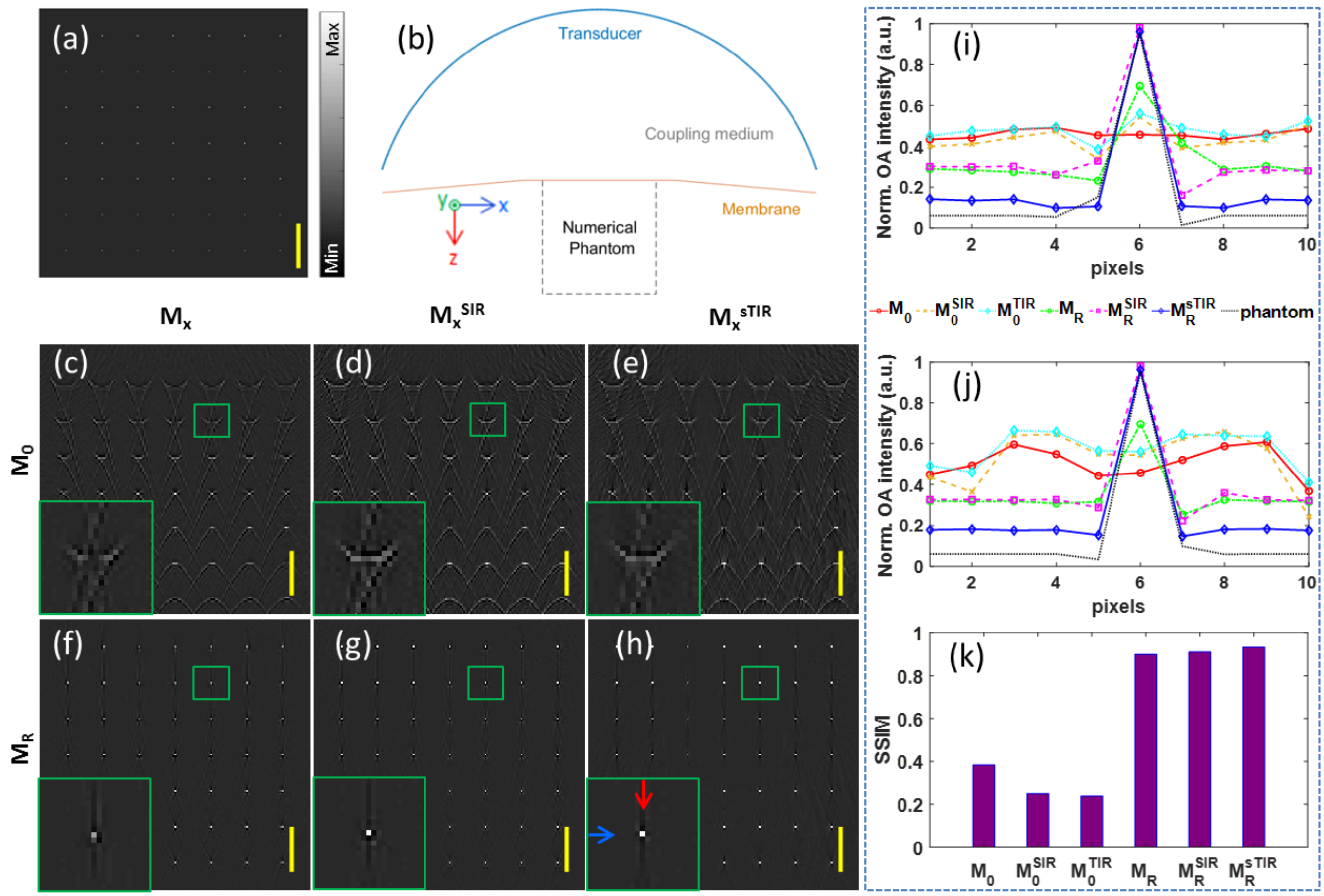

Fig. 4. **Numerical simulation to demonstrate adverse effects on image quality due to neglecting transducer properties.** A dot grid (optical absorbers) was simulated for the 30 x 30 mm field of view of a handheld probe, and noise-less signals were assumed. (a) Numerical phantom with dot pattern. (b) Schematic of the setup of dot grid pattern being scanned with the handheld probe. (c-h) Images of the grid pattern reconstructed using the M_0 forward model (upper row) or M_R forward model (lower row) in the absence of transducer correction geometry (left column), with SIR correction (middle column) or sTIR correction (right column). The red and blue arrows indicate axial and lateral line profiles. Insets show higher-magnification views of the reconstruction area boxed in green. (i-j) Axial (upper) and lateral (lower) line profiles across images reconstructed using M_0, M_0^{SIR}, M_0^{sTIR}, M_R, M_R^{SIR}, M_R^{sTIR} and phantom. (k) Structural similarity indices(SSIMs) of reconstructions using all six models. Scale bar, 5 mm.

signals were detected using a toroidal concave array transducer (Imasonic, France) with 256 elements along an arc spanning 145°. The radius of the transducer array was 60 mm, while each element was cylindrically focused in the azimuthal plane or image plane (xz-plane) with a radius of curvature of 65 mm. Each element had a chord height (in elevation) of 26 mm, width of 0.49 mm and kerf (inter-element spacing) of 0.1 mm. The center frequency of the transducer was 4 MHz with a bandwidth (-6 dB) of 50% in transmit/receive mode. The active side of the handheld probe was sealed with optically and acoustically transparent low-density polyethylene membrane for suitable handheld operation, and the cavity between the membrane and the concave transducer was filled with heavy water (D_2O) for acoustic coupling. A custom-built 256-channel analog-to-digital converter was used to digitize the transducer signals at a sampling rate of 40 MS/s with an amplitude resolution of 12-bits. Each laser pulse triggers the data acquisition in a single-frame-per-pulse fashion, which makes the system capable of scanning multiple wavelengths rapidly.

Two phantoms were imaged using the handheld probe immersed in water. Fig. 3b-c presents the first phantom, which was built to characterize the sTIR of the system and also experimentally measure the resolution of the system. A single polyethylene microsphere of diameter 100 μm was embedded inside a cylinder of 1.5% (w/v) agar cylinder. Fig. 5a-c depicts the second phantom consisting of a dot grid (7 × 7) printed on a piece of white paper (30 mm × 30 mm) with black ink and embedded in 1.5% (w/v) agar. The dots were approximately 200 μm in diameter with a spacing of 4 mm. All phantom measurements were performed at 700 nm illumination. Two clinical scans were performed non-invasively on the arms of healthy volunteers using the handheld probe. Informed consent was received before volunteers were scanned. Regular ultrasound gel was used in between the membrane of the probe and the skin to couple optically generated acoustic waves from tissue into the probe.

IV. Results

Equipped with this sTIR forward model, we first investigated how our proposed model improves the system resolution.

This article has been accepted for publication in a future issue of this journal, but has not been fully edited. Content may change prior to final publication. Citation information: DOI 10.1109/TMI.2020.2989236, IEEE Transactions on Medical Imaging

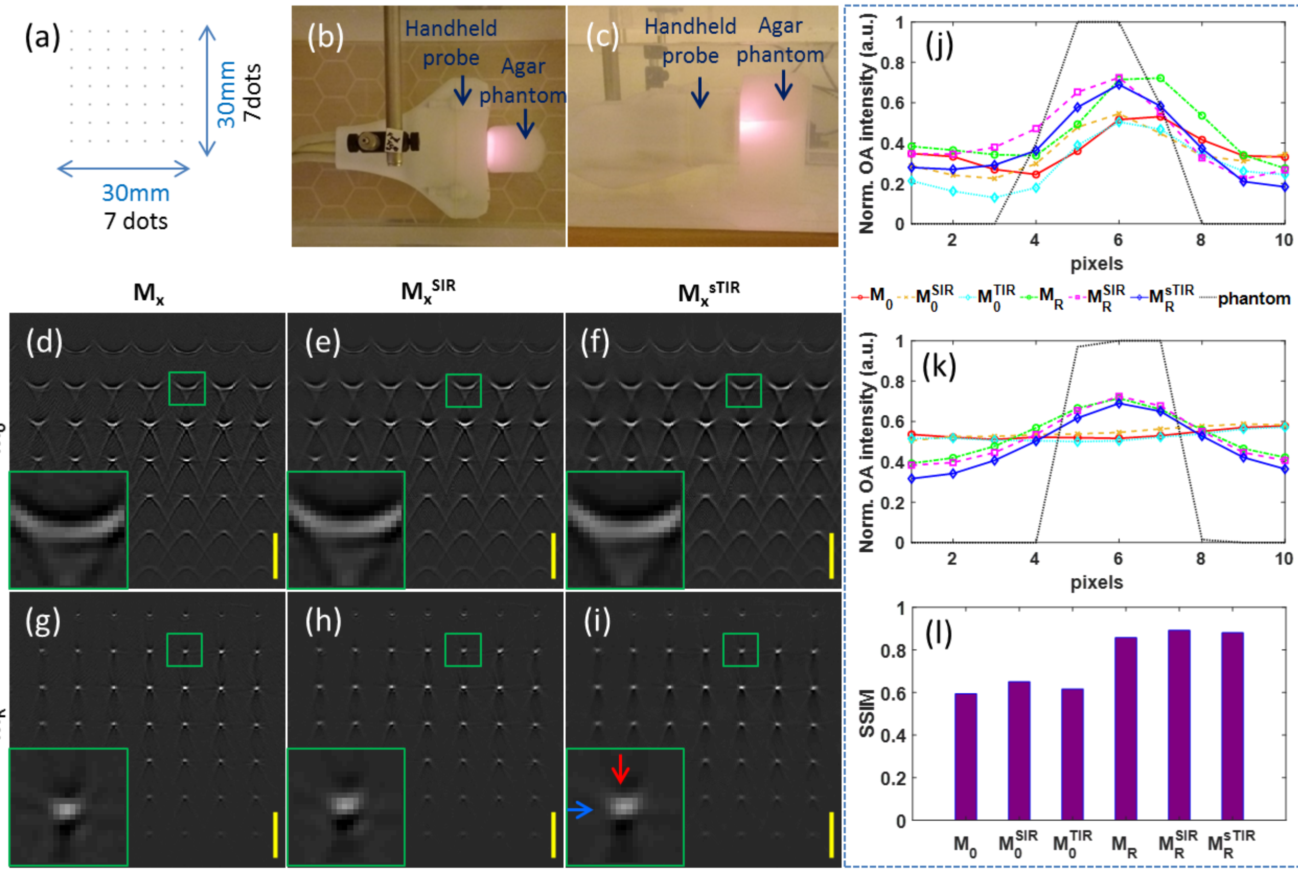

Fig. 5. Improved reconstruction of a printed phantom through correcting for refraction and transducer properties. A dot grid was printed on a piece of white paper and embedded in agar and scanned with the handheld probe immersed in water using single excitation wavelength of 700 nm. (a) Schematic of the dot pattern. (b-c) Photographs of the agar phantom being scanned with the handheld probe. (d-i) Images of the printed phantom reconstructed using the $\boldsymbol{M_0}$ forward model (upper row) or $\boldsymbol{M_R}$ forward model (lower row) in the absence of transducer correction geometry (left column), with SIR correction (middle column) or sTIR correction (right column). The red and blue arrows indicate axial and lateral line profiles. Insets show higher-magnification views of the reconstruction area boxed in green. (j-k) Axial (upper) and lateral (lower) line profiles across images reconstructed using the models $\boldsymbol{M_0}$, $\boldsymbol{M_0^{SIR}}$, $\boldsymbol{M_0^{sTIR}}$, $\boldsymbol{M_R}$, $\boldsymbol{M_R^{SIR}}$, $\boldsymbol{M_R^{sTIR}}$ or phantom (ground truth). (l) Structural similarity indices of reconstructions performed using all six models. Scale bar, 5 mm.

Then we tested the sTIR model on numerical phantoms and thereafter we validated the performance of the forward sTIR model with a physical agar phantom. In all cases we present reconstruction results using all six forward models in Table I to evaluate the performance of each correction stage of the forward TIR model. Finally, we tested the performance of the proposed sTIR models on clinical data recorded from human volunteers. Additional results from numerical phantoms with added noise are available in Supplementary Figs. 1-2.

A. Characterization of system resolution

We examined the ability of the proposed sTIR corrected reconstruction to improve system resolution beyond acoustic models assuming constant speed of propagation. We scanned a microsphere of diameter 100 µm (sub-resolution dimension) at two locations, namely the region of interest $\mathrm{ROI_A}$ in the upper half of the FOV and $\mathrm{ROI_B}$ in the center of the FOV as shown in Fig. 3a. Fig. 3b shows the photograph of the setup of the microsphere being scanned by the handheld probe, while Fig. 3c presents a schematic of the microsphere phantom. Fig. 3d shows reconstruction of the microsphere phantom at $\mathrm{ROI_A}$ based on the M_0 model. As expected we found strong artefacts due to mismatch in local acoustic speed. Fig. 3e-f show reconstructions based, respectively, on M_0^{SIR} and M_0^{sTIR}, in which artefacts are still present. Fig. 3g shows that M_R-based modelling generates a reconstruction that mitigates these artefacts, and Fig. 3h-i show improved resolution with M_R^{SIR} and M_R^{sTIR} reconstruction. Fig. 3j compares the lateral and axial full width at half-maximum (FWHM) for images of $\mathrm{ROI_A}$, reconstructed using all six models. Resolution increases with SIR and sTIR correction in general, although the $\mathrm{ROI_A}$ refraction model could not significantly enhance resolution, probably because of membrane modelling inaccuracy. Fig. 3k-p shows reconstructed images of the microsphere phantom at $\mathrm{ROI_B}$ based on all six models. We again observe strong artefacts caused in M_0-based reconstruction, which SIR and sTIR correction fails to mitigate. Fig. 3n shows that refraction correction mitigates artefacts, and Fig. 3o-p shows improvement in the microsphere's resolution and isotropic shape following SIR and sTIR correction. Fig. 3q compares the lateral and axial FWHM values for reconstructed images at ROI_B showing a monotonic increase in lateral resolution using six models. Axial resolution increases monotonically with SIR and sTIR correction. Comparison of lateral-axial resolutions of M_0 and M_R demonstrates that refraction correction preserves the isotropic shape of absorbers. M_R^{sTIR} reconstruction achieves an axial resolution around 200 µm.

B. Reconstruction test using numerical phantoms

Equipped with the comprehensive entire-probe sTIR forward model, we performed reconstruction of a numerical phantom using the same six models as in the previous section. Fig. 4a displays the ground truth of the numerical phantom with simulated dot grid pattern of optical absorbers in the image plane. The setup of the numerical phantom being scanned by the handheld probe is illustrated in Fig. 4b. Fig. 4c displays the reconstructed image of the numerical phantom using M_0 model. It is observed that the dot absorbers are significantly distorted and the degree of distortion is spatially variant, with highest degradation at the upper and lower corners of the image and least degradation at the centre of the image. The reconstructed images of the numerical phantom using M_0^{SIR} and M_0^{sTIR}, are shown in Fig. 4d and 4e, respectively. It is evident that SIR and sTIR correction fails to improve on Fig. 4c, because of the presence of stronger artefacts caused by mismatch of acoustic speed (between heavy water and phantom). Fig. 4f shows the reconstruction with M_R ; the zoomed-in region of the reconstructed image indicates that refraction modelling resolves the dot absorbers more accurately throughout the FOV. Fig. 4g shows the reconstructed image with M_R^{SIR} of the numerical dot-grid phantom. Comparison of the inset in Fig. 4g with that in Fig. 4f indicates that the M_R^{SIR} reconstruction mitigates the distortion effects caused by the transducer's physical dimensions. Finally, Fig. 4h shows the phantom image reconstructed using M_R^{sTIR}; isotropic shape improvement is observed in the inset of Fig. 4h. Fig. 4i and 4j compare, respectively, the axial and lateral profiles through absorbers reconstructed using all six models (Fig. 4c-h) along with the ground truth or phantom shown in Fig. 4a. In both the axial and lateral dimensions, the M_R^{sTIR} reconstruction accurately localizes the absorbers, while the M_0 reconstruction distorts the localization information more on the axial dimension than on the lateral dimension. Fig 4k compares the structural similarity indices of images reconstructed with all six models and demonstrates that the refraction model enhances the structural similarity in general, and that SIR and sTIR correction further increases structural similarity.

C. Experimental validation with phantoms

As a next step, we validated the performance of our reconstruction method using physical phantoms. Fig. 5a shows the dot pattern that was printed on paper and embedded in agar. Fig. 5b-c show top and side views, respectively, of the phantom. Fig. 5d displays the cross-section image reconstructed using constant acoustic speed model-based reconstruction (M_0). The distortion due to local mismatch of acoustic speed is observed across the entire FOV. Fig. 5e and 5f show reconstructions using M_0^{SIR} or M_0^{sTIR}. SIR correction and TIR correction with constant acoustic speed fail to show improvement in the presence of strong distortion due to acoustic speed mismatch. In contrast, Fig. 5g shows that M_R-based reconstruction provides much better shape and localization of the optical absorbers. Fig. 5h-i show SIR and sTIR correction, respectively, in refraction model-based reconstruction. Comparison of the inset in Fig. 5g with that in Fig. 5h indicates that the SIR correction improves distortion effects caused by transducer geometry. Shape and contrast improvement is observed in the inset of Fig. 5i. Fig. 5j and 5k compare, respectively, the axial and lateral profiles through the dots, reconstructed using all six models (Fig. 5d-i), along with the phantom. Here, M_0 reconstruction distorts lateral localization less than axial localization. Consistent with these comparisons, Fig. 5l shows a much better structural similarity index for refraction based models with M_R^{sTIR} showing highest similarity with respect to ground truth or phantom. The similar structural similarity index for M_R^{SIR} and M_R is attributed to factors such as noise and inaccuracy of the membrane model.

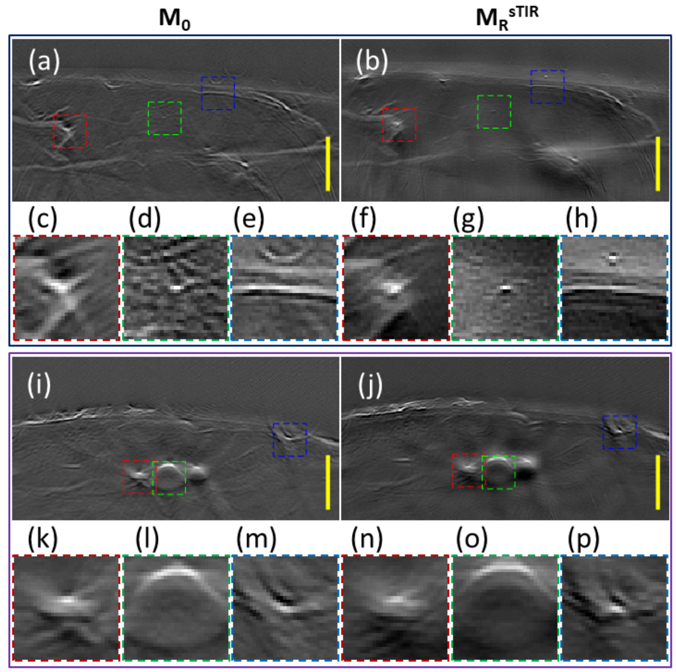

Fig. 6. Improvement in clinical imaging through correcting for refraction and transducer properties. Healthy volunteers were imaged non-invasively using the MSOT handheld probe at two locations on the arm using single excitation wavelength of 800 nm. (a-b) Reconstructions of Scan 1 using $\boldsymbol{M_0}$ and $\boldsymbol{M_R^{sTIR}}$. (c-e) and (f-h) are zoomed-in images of locations marked with red, green and blue inside panels a and b respectively, where the $\boldsymbol{M_R^{sTIR}}$ model improved vascular structure. (i-j) Reconstructions of Scan 2 using $\boldsymbol{M_0}$ and $\boldsymbol{M_R^{sTIR}}$. (k-m) and (n-p) are zoomed-in images of locations marked with red, green and blue inside panels i and j respectively, where the $\boldsymbol{M_R^{sTIR}}$ model improved vascular structure. Scale bar, 5 mm.

D. Clinical measurements

In order to move beyond phantoms and closer to the clinic, we examined whether our proposed M_R^{sTIR} model could improve the reconstruction quality of clinical data in comparison to the constant acoustic speed M_0 model-based reconstruction.

Two locations of human forearm were scanned, named Scan 1 and Scan 2. These regions were selected because they contain many shallow vessels that are good optical absorbers [54], [55]. Fig. 6a shows the cross-sectional tomographic reconstruction of the data acquired in Scan 1, using model M_0, which involves constant acoustic speed model without TIR correction. The acoustic speed was chosen manually to optimize the image quality. Numerous small and medium-sized vessels are observed, though they appear to be distorted. Fig. 6b shows the corresponding reconstruction using M_R^{sTIR}, and panels c-e and f-h show magnified views of locations marked in red, green and blue boxes indicating improvement in representation of vascular structures. Comparing panels c and f we easily observe improvement in structural quality on using sTIR reconstruction. Comparison of panels d and g we observe that the sTIR correction reduces background noise retaining the sharp vascular edges. Also, comparing the cross-section and lateral vessels in panels e and h we observe that sTIR not only improves structural quality but also slightly improves resolution of small vessels around 200 µm, indicating the usefulness of the proposed model for microvascular imaging. Then we used our sTIR-model to target the radial artery in the wrist (Scan 2). Fig. 6i shows the reconstruction of Scan 2 using M_0, in which a clear distortion of the radial artery (panel l) is observed, due to mismatch in acoustic speed. As before, the acoustic speed was chosen manually to optimize the image quality. Fig. 6j shows a reconstruction of Scan 2, using M_R^{sTIR} or sTIR correction demonstrating some improvement in the represented structure of the radial artery (green box) and other vascular structures. The arterial cross section is likely to be elliptical because of the small amount of pressure applied by the probe onto the wrist and this is expected to be recovered by sTIR correction. However, comparing the zoomed-in panels k-m and n-p we observe that the image quality improvement in Scan 2 is not as strong as we observed in Scan 1. This is probably because due to deformation of membrane from flat to curved as we observe comparing the Scans 1 and 2. Overall, it is observed that with sTIR correction, the vessels have more natural shape, while the skin line is free of artefacts, demonstrating superior image quality. Reconstruction of Scans 1 and 2 for all six models are additionally available in Supplementary Fig. 3.

The proposed sTIR corrected reconstruction is shown to give the best spatial resolution, without refraction artefacts throughout the field of view, for an optimal pair of acoustic speeds in tissue and coupling medium. For constant acoustic speed models, the wavefronts do not converge at all, and hence cannot eliminate the refraction-based artefacts. This is demonstrated using the dot-grid physical phantom experiments. Hence, one has to properly tune the c_0 value to enable convergence of the optoacoustic wavefronts at different parts of the field of view simultaneously. In this work, the proposed sTIR model reliably offers accurate reconstruction throughout the FOV. In order to demonstrate this robustness feature, we reconstruct Scan 1 with acoustic speeds c_t=1450m/s, 1455m/s and 1460m/s as shown in Fig. 7d-f, varying the value compared to the reference value c_t=1455m/s. Fig. 7a-c compare the M_0 based reconstructions for c_0=1410m/s, 1415m/s and 1420m/s, varying the value compared to the reference c_0=1415m/s. Using the proposed scheme, the vascular structures are less distorted than the reconstructions using M_0 reconstructions. In other words, the wavefront converges better with the proposed M_R^{sTIR} compared to using M_0, as expected.

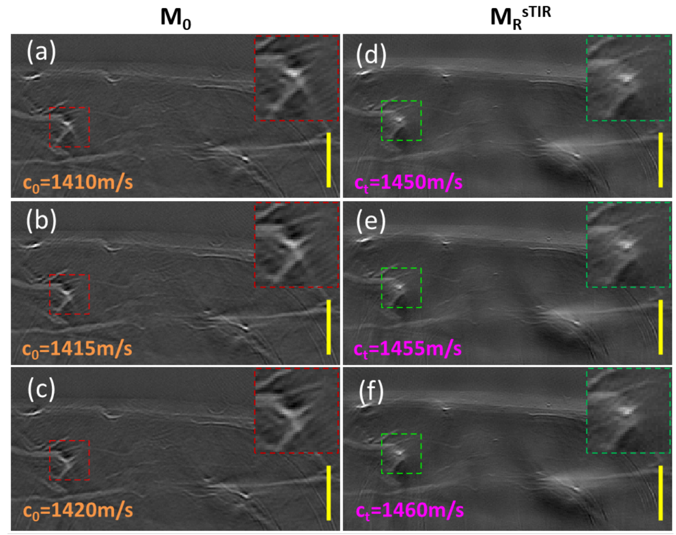

Fig. 7. Robustness of M_0 and M_R^{sTIR} models against slight variation in acoustic speed. (a-c) M_0 reconstructions of Scan 1 using c_0=1410 m/s, 1415 m/s and 1420 m/s respectively. (d-f) M_R^{sTIR} reconstructions of Scan 1 using c_t=1450 m/s, 1455 m/s and 1460 m/s respectively. Insets with red and green dashed border are magnified views of highlighted exemplary vessel showing M_R^{sTIR} reconstruction is more robust than M_0 reconstruction to slight change in acoustic speed used in reconstruction. Scale bar, 5 mm.

V. Discussion

In this work, we measured the TIR of an optoacoustic handheld scanning probe in sparse locations and modelled it in the full FOV, using a geometric acoustics SIR model. We verified the correctness of our model by showing that the derived EIR is independent of the impulse origin. Hence, we proved that combining the derived EIR with the modelled SIR yields a full FOV characterization of sTIR that takes into account the acoustic mismatch at the interface between sample and coupling medium. Incorporating the sTIR into the model-based reconstruction algorithm, we demonstrated a significant improvement in resolution and reconstruction accuracy throughout the FOV with experimental measurements. In order to systematically demonstrate the effects of the components of the sTIR, namely - refraction, SIR and EIR, we considered the sequence of phenomena from the generation of the acoustic impulse until conversion to an electrical signal. First, the refraction affects the time of flight of the generated acoustic impulse. Second, the acoustic wave is averaged on the surface of the detector which is modelled in the SIR. Third, the conversion of acoustic pressure into electrical signal is modelled as the EIR. We considered three refraction based forward models: for pure refraction correction, for correction of refraction dependent SIR, and for full refraction dependent sTIR. We also considered the corresponding three constant acoustic speed models to study the effect of refraction correction. In total, we use the six different models to demonstrate our experimental results. In the case of physical phantoms, the improvement in structural similarity index was five-fold over a conventional model that assumed a point detector and constant acoustic speed.

We observed that the spatially varying component, SIR, depends on the refraction of acoustic waves at the interface of coupling medium and tissue due to a mismatch in acoustic speed. In heavy water at room temperature the acoustic speed is roughly 1397 m/s [46], which is quite different from the average acoustic speed in soft tissue (1540 m/s [47]). Hence, we develop a forward model taking into account this acoustic refraction at the probe membrane and the SIR of the transducer to reconstruct distortion-free images and achieve uniform accuracy throughout the FOV, which was not possible with existing model-based reconstruction that assumed constant acoustic speed. From the results of phantom experiments, we observe that the refraction of acoustic waves causes greater distortion in the reconstructed images than SIR- and EIR-based distortion arising from the configuration of our handheld probe.

It is to be noted that the use of heavy water might be advantageous because it absorbs near-infrared light less than important endogenous chromophores such as hemoglobin, lipids and normal water [55], [56]. Our proposed work will eventually facilitate the use of heavy water-filled handheld scanning probes for detailed functional and metabolic imaging in the future.

Our sTIR correction model enhanced the lateral and axial resolutions at the center of the FOV by 54% and 37%, respectively, resulting in approximate lateral resolution of 230 μm and axial resolution of 200 μm. Clinical measurements demonstrated that we could visualize vessels as small as 200 μm in diameter at depths of 1.5 cm in the clinical measurements with good accuracy. This will facilitate imaging of small vessels deeper under the skin to study health and understand changes in blood vessels caused by disease [57], [58].

We showed results for one fixed membrane model. However, in clinical measurements, when the handheld probe is pressed against the human body to ensure perfect contact with the skin, the non-rigid membrane sealing the heavy water deforms slightly according to the skin curvature. This leads to minor distortions of the resolved structures in the tissue close to the membrane up to a depth of around 4mm. The change in the membrane contour does not severely affect the recovery of deeper structures. For longitudinal clinical studies concerning optoacoustic features of subcutaneous fat, blood vessels, and muscle tissue we believe a fixed model is robust enough for most purposes. Building the sTIR model for a particular membrane model is computationally expensive and needs to be optimized. Hence, flexible models adaptive to complex membrane shapes can be explored in the future. Also, effects of laser excitation impulse response, attenuation of light and ultrasound etc. can be added to estimate exact EIR of the system. Currently, the computation of the SIR and refraction in the whole FOV are performed sequentially. These computations can be accelerated using GPUs. As a further extension of the method, we will consider correcting for heterogeneous acoustic speed distributions inside the tissue alongside modelling transducer and laser excitation.

In summary, we found that refraction plays a major role in the appearance of strong artefacts arising due to mismatch in acoustic speed and its correction results in images of higher accuracy. SIR correction slightly improves the reconstructed shapes of absorbers, although the magnitude of this improvement may be weakened by other experimental errors. Finally, EIR correction improves the image resolution and contrast. Overall, corrections based on the presented sTIR model delivered images of higher resolution deeper in tissue, enabling improved visualization of not only bulk tissue but also finer vascular networks for biomedical research and clinical applications.

Acknowledgment

All authors thank A. Chapin Rodríguez, PhD for proofreading the manuscript.

References

[1] P. Burgholzer, G. J. Matt, M. Haltmeier, and G. Paltauf, "Exact and approximative imaging methods for photoacoustic tomography using an arbitrary detection surface," *Phys. Rev. E*, vol. 75, p. 046706, Apr 2007.

[2] K. Wang, S. A. Ermilov, R. Su, H. Brecht, A. A. Oraevsky, and M. A. Anastasio, "An imaging model incorporating ultrasonic transducer properties for three-dimensional optoacoustic tomography," *IEEE Transactions on Medical Imaging*, vol. 30, no. 2, pp. 203–214, Feb 2011.

[3] G. Paltauf, P. R. Torke, and R. Nuster, "Modeling photoacoustic imaging with a scanning focused detector using Monte Carlo simulation of energy deposition," *Journal of Biomedical Optics*, vol. 23, no. 12, pp. 1 – 11, 2018.

[4] C. Huang, K. Wang, L. Nie, L. V. Wang, and M. A. Anastasio, "Full-wave iterative image reconstruction in photoacoustic tomography with acoustically inhomogeneous media," *IEEE Transactions on Medical Imaging*, vol. 32, no. 6, pp. 1097–1110, June 2013.

[5] T. Berer, I. A. Veres, H. Grün, J. Bauer-Marschallinger, K. Felbermayer, and P. Burgholzer, "Characterization of broadband fiber optic line detectors for photoacoustic tomography," *Journal of Biophotonics*, vol. 5, no. 7, pp. 518–528, 2012.

[6] S. Bu, Z. Liu, T. Shiina, K. Kondo, M. Yamakawa, K. Fukutani, Y. Someda, and Y. Asao, "Model-based reconstruction integrated with fluence compensation for photoacoustic tomography," *IEEE Transactions on Biomedical Engineering*, vol. 59, no. 5, pp. 1354–1363, May 2012.

[7] J. Zhang, M. A. Anastasio, P. J. La Riviere, and L. V. Wang, "Effects of different imaging models on least-squares image reconstruction accuracy in photoacoustic tomography," *IEEE Transactions on Medical Imaging*, vol. 28, no. 11, pp. 1781–1790, Nov 2009.

[8] B. T. Cox, S. R. Arridge, and P. C. Beard, "Photoacoustic tomography with a limited-aperture planar sensor and a reverberant cavity," *Inverse Problems*, vol. 23, no. 6, pp. S95–S112, nov 2007.

[9] A. Rosenthal, V. Ntziachristos, and D. Razansky, "Model-based optoacoustic inversion with arbitrary-shape detectors," *Medical Physics*, vol. 38, no. 7, pp. 4285–4295, 2011.

[10] M. W. Schellenberg and H. K. Hunt, "Hand-held optoacoustic imaging: A review," *Photoacoustics*, vol. 11, pp. 14 – 27, 2018.

[11] S. Liu, X. Feng, H. Jin, R. Zhang, Y. Luo, Z. Zheng, F. Gao, and Y. Zheng, "Handheld photoacoustic imager for theranostics in 3d," *IEEE Transactions on Medical Imaging*, vol. 38, no. 9, pp. 2037–2046, Sep. 2019.

[12] Y. Han, L. Ding, X. L. D. Ben, D. Razansky, J. Prakash, and V. Ntziachristos, "Three-dimensional optoacoustic reconstruction using fast sparse representation," *Opt. Lett.*, vol. 42, no. 5, pp. 979–982, Mar 2017.

[13] J. Prakash, S. Mandal, D. Razansky, and V. Ntziachristos, "Maximum entropy based non-negative optoacoustic tomographic image reconstruction," *IEEE Transactions on Biomedical Engineering*, vol. 66, no. 9, pp. 2604–2616, Sep. 2019.

[14] X. L. Dean-Ben, V. Ntziachristos, and D. Razansky, "Acceleration of optoacoustic model-based reconstruction using angular image discretization," *IEEE Transactions on Medical Imaging*, vol. 31, no. 5, pp. 1154–1162, May 2012.

[15] J. Kim, J. Y. Kim, S. Jeon, J. W. BAIK, S. H. Cho, and C. Kim, "Super-resolution localization photoacoustic microscopy using intrinsic red blood cells as contrast absorbers," *Light: Science & Applications*, vol. 8, no. 1, p. 103, 2019.

[16] R. A. Kruger, P. Liu, Y. R. Fang, and C. R. Appledorn, "Photoacoustic ultrasound (paus)—reconstruction tomography," *Medical Physics*, vol. 22, no. 10, pp. 1605–1609, 1995.

[17] V. G. Andreev, A. A. Karabutov, S. V. Solomatin, E. V. Savateeva, V. Aleinikov, Y. V. Zhulina, R. D. Fleming, and A. A. Oraevsky, "Optoacoustic tomography of breast cancer with arc-array transducer," in *Biomedical Optoacoustics*, A. A. Oraevsky, Ed., vol. 3916, International Society for Optics and Photonics. SPIE, 2000, pp. 36 – 47.

[18] A. Rosenthal, D. Razansky, and V. Ntziachristos, "Fast semi-analytical model-based acoustic inversion for quantitative optoacoustic tomography," *IEEE Transactions on Medical Imaging*, vol. 29, no. 6, pp. 1275–1285, June 2010.

[19] M. Xu and L. V. Wang, "Analytic explanation of spatial resolution related to bandwidth and detector aperture size in thermoacoustic or photoacoustic reconstruction," *Phys. Rev. E*, vol. 67, p. 056605, May 2003.

[20] T. D. Khokhlova, I. M. Pelivanov, and A. A. Karabutov, "Optoacoustic tomography utilizing focused transducers: The resolution study," *Applied Physics Letters*, vol. 92, no. 2, p. 024105, 2008.

[21] M. Haltmeier and G. Zangerl, "Spatial resolution in photoacoustic tomography: effects of detector size and detector bandwidth," *Inverse Problems*, vol. 26, no. 12, p. 125002, oct 2010.

[22] N. A. Rejesh, H. Pullagurla, and M. Pramanik, "Deconvolution-based deblurring of reconstructed images in photoacoustic/thermoacoustic tomography," *J. Opt. Soc. Am. A*, vol. 30, no. 10, pp. 1994–2001, Oct 2013.

[23] D. Van de Sompel, L. S. Sasportas, J. V. Jokerst, and S. S. Gambhir, "Comparison of deconvolution filters for photoacoustic tomography," *PLOS ONE*, vol. 11, no. 3, pp. 1–28, 03 2016.

[24] K. Mitsuhashi, K. Wang, and M. A. Anastasio, "Investigation of the far-field approximation for modeling a transducer's spatial impulse response in photoacoustic computed tomography," *Photoacoustics*, vol. 2, no. 1, pp. 21 – 32, 2014.

[25] M.-L. Li and C.-C. Cheng, "Reconstruction of photoacoustic tomography with finite-aperture detectors: deconvolution of the spatial impulse response," in *Photons Plus Ultrasound: Imaging and Sensing 2010*, A. A. Oraevsky and L. V. Wang, Eds., vol. 7564, International Society for Optics and Photonics. SPIE, 2010, pp. 619 – 624.

[26] V. Neuschmelting, N. C. Burton, H. Lockau, A. Urich, S. Harmsen, V. Ntziachristos, and M. F. Kircher, "Performance of a multispectral optoacoustic tomography (msot) system equipped with 2d vs. 3d hand-held probes for potential clinical translation," *Photoacoustics*, vol. 4, no. 1, pp. 1 – 10, 2016.

[27] A. Karlas, N.-A. Fasoula, K. Paul-Yuan, J. Reber, M. Kallmayer, D. Bozhko, M. Seeger, H.-H. Eckstein, M. Wildgruber, and V. Ntziachristos, "Cardiovascular optoacoustics: From mice to men – a review," *Photoacoustics*, vol. 14, pp. 19 – 30, 2019.

[28] X. L. Deán-Ben, A. Özbek, and D. Razansky, "Accounting for speed of sound variations in volumetric hand-held optoacoustic imaging," *Frontiers of Optoelectronics*, vol. 10, no. 3, pp. 280–286, Sep 2017.

[29] J. Kim, S. Park, Y. Jung, S. Chang, J. Park, Y. Zhang, J. F. Lovell, and C. Kim, "Programmable Real-time Clinical Photoacoustic and Ultrasound Imaging System," *Scientific Reports*, vol. 6, no. September, pp. 1–11, 2016.

[30] M. Heijblom, W. Steenbergen, and S. Manohar, "Clinical photoacoustic breast imaging: The twente experience." *IEEE Pulse*, vol. 6, no. 3, pp. 42–46, May 2015.

[31] P. K. Upputuri and M. Pramanik, "Recent advances toward preclinical and clinical translation of photoacoustic tomography: a review," *Journal of Biomedical Optics*, vol. 22, no. 4, pp. 1 – 19, 2016.

[32] W. J. K. Valluru Keerthi S., "Clinical photoacoustic imaging of cancer," *Ultrasonography*, vol. 35, no. 4, pp. 267–280, 2016.

[33] W. Choi, E.-Y. Park, S. Jeon, and C. Kim, "Clinical photoacoustic imaging platforms," *Biomedical Engineering Letters*, vol. 8, no. 2, pp. 139–155, May 2018.

[34] I. Steinberg, D. M. Huland, O. Vermesh, H. E. Frostig, W. S. Tummers, and S. S. Gambhir, "Photoacoustic clinical imaging," *Photoacoustics*, vol. 14, pp. 77 – 98, 2019.

[35] Y. Zhou, G. Li, L. Zhu, C. Li, L. A. Cornelius, and L. V. Wang, "Handheld photoacoustic probe to detect both melanoma depth and volume at high speed in vivo," *Journal of Biophotonics*, vol. 8, no. 11-12, pp. 961–967, 2015.

[36] B. T. Cox, S. Kara, S. R. Arridge, and P. C. Beard, "k-space propagation models for acoustically heterogeneous media: Application to biomedical photoacoustics," *The Journal of the Acoustical Society of America*, vol. 121, no. 6, pp. 3453–3464, 2007.

[37] L. V. Wang, "Tutorial on photoacoustic microscopy and computed tomography," *IEEE Journal of Selected Topics in Quantum Electronics*, vol. 14, no. 1, pp. 171–179, Jan 2008.

[38] K. Wang, R. Su, A. A. Oraevsky, and M. A. Anastasio, "Investigation of iterative image reconstruction in three-dimensional optoacoustic tomography," *Physics in Medicine and Biology*, vol. 57, no. 17, pp. 5399–5423, aug 2012.

[39] G. J. Diebold, T. Sun, and M. I. Khan, "Photoacoustic monopole radiation in one, two, and three dimensions," *Phys. Rev. Lett.*, vol. 67, pp. 3384–3387, Dec 1991.

[40] G. E. Forsythe, M. A. Malcolm, and C. B. Moler, *Computer Methods for Mathematical Computations*. Prentice Hall Professional Technical Reference, 1977.

[41] R. P. Brent, *Algorithms for Minimization without Derivatives*, 1st ed. New Jersey: Prentice-Hall, 1973.

[42] B. R. Rao, "Dispersion of sound velocity in liquids," *Nature*, p. 885, May 1937.

[43] Y. Levy, Y. Agnon, and H. Azhari, "Measurement of speed of sound dispersion in soft tissues using a double frequency continuous wave method," *Ultrasound in Medicine and Biology*, vol. 32, no. 7, pp. 1065 – 1071, 2006.

[44] M. Verweij, B. Treeby, K. van Dongen, and L. Demi, "2.19 - simulation of ultrasound fields," in *Comprehensive Biomedical Physics*, A. Brahme, Ed. Oxford: Elsevier, 2014, pp. 465 – 500.

[45] J. A. Jensen, "Field: A program for simulating ultrasound systems," in *10TH NORDICBALTIC CONFERENCE ON BIOMEDICAL IMAGING, VOL. 4, SUPPLEMENT 1, PART 1:351–353*, 1996, pp. 351–353.

[46] W. D. Wilson, "Speed of sound in heavy water as a function of temperature and pressure," *The Journal of the Acoustical Society of America*, vol. 33, no. 3, pp. 314–316, 1961.

[47] R. C. Chivers and R. J. Parry, "Ultrasonic velocity and attenuation in mammalian tissues," *The Journal of the Acoustical Society of America*, vol. 63, no. 3, pp. 940–953, 1978.

[48] M. Á. Araque Caballero, A. Rosenthal, J. Gateau, D. Razansky, and V. Ntziachristos, "Model-based optoacoustic imaging using focused detector scanning," *Optics Letters*, vol. 37, no. 19, p. 4080, 2012.

[49] J. Prakash and P. K. Yalavarthy, "A lsqr-type method provides a computationally efficient automated optimal choice of regularization parameter in diffuse optical tomography," *Medical Physics*, vol. 40, no. 3, p. 033101, 2013.

[50] C. B. Shaw, J. Prakash, M. Pramanik, and P. K. Yalavarthy, "Least squares QR-based decomposition provides an efficient way of computing optimal regularization parameter in photoacoustic tomography," *Journal of Biomedical Optics*, vol. 18, no. 8, pp. 1 – 4, 2013.

[51] Zhou Wang, A. C. Bovik, H. R. Sheikh, and E. P. Simoncelli, "Image quality assessment: from error visibility to structural similarity," *IEEE Transactions on Image Processing*, vol. 13, no. 4, pp. 600–612, April 2004.

[52] G. Diot, S. Metz, A. Noske, E. Liapis, B. Schroeder, S. V. Ovsepian, R. Meier, E. Rummeny, and V. Ntziachristos, "Multispectral optoacoustic tomography (msot) of human breast cancer," *Clinical Cancer Research*, vol. 23, no. 22, pp. 6912–6922, 2017.

[53] A. Buehler, M. Kacprowicz, A. Taruttis, and V. Ntziachristos, "Real-time handheld multispectral optoacoustic imaging," *Opt. Lett.*, vol. 38, no. 9, pp. 1404–1406, May 2013.

[54] A. Karlas, J. Reber, G. Diot, D. Bozhko, M. Anastasopoulou, T. Ibrahim, M. Schwaiger, F. Hyafil, and V. Ntziachristos, "Flow-mediated dilatation test using optoacoustic imaging: a proof-of-concept," *Biomed. Opt. Express*, vol. 8, no. 7, pp. 3395–3403, Jul 2017.

[55] A. Buehler, G. Diot, T. Volz, J. Kohlmeyer, and V. Ntziachristos, "Imaging of fatty tumors: appearance of subcutaneous lipomas in optoacoustic images," *Journal of Biophotonics*, vol. 10, no. 8, pp. 983–989, 2017.

[56] S. L. Jacques, "Optical properties of biological tissues: a review," *Physics in Medicine and Biology*, vol. 58, no. 11, pp. R37–R61, may 2013.

[57] J. S. Pober and W. C. Sessa, "Inflammation and the blood microvascular system," *Cold Spring Harbor Perspectives in Biology*, vol. 7, no. 1, 2015.

[58] M. J. Fowler, "Microvascular and macrovascular complications of diabetes," *Clinical Diabetes*, vol. 26, no. 2, pp. 77–82, 2008.